ISPRS Journal of Photogrammetry and Remote Sensing 134 (2017) 135–147

Contents lists available at ScienceDirect

ISPRS Journal of Photogrammetry and Remote Sensing

journal homepage: www.elsevier.com/locate/isprsjprs

# DEM generation from contours and a low-resolution DEM

Xinghua Li [a], Huanfeng Shen [b,c,*], Ruitao Feng [b], Jie Li [d], Liangpei Zhang [e,c]

[a] School of Remote Sensing and Information Engineering, Wuhan University, PR China
[b] School of Resource and Environmental Sciences, Wuhan University, PR China
[c] Collaborative Innovation Center for Geospatial Information Technology, PR China
[d] School of International Software, Wuhan University, PR China
[e] State Key Laboratory of Information Engineering in Surveying, Mapping, and Remote Sensing, Wuhan University, PR China

ARTICLE INFO

*Article history:*
Received 12 January 2017
Received in revised form 25 August 2017
Accepted 20 September 2017
Available online 11 November 2017

*Keywords:*
Contours
Dictionary learning
Digital elevation model (DEM)
Sparse representation
Spatial regularization

ABSTRACT

A digital elevation model (DEM) is a virtual representation of topography, where the terrain is established by the three-dimensional co-ordinates. In the framework of sparse representation, this paper investigates DEM generation from contours. Since contours are usually sparsely distributed and closely related in space, sparse spatial regularization (SSR) is enforced on them. In order to make up for the lack of spatial information, another lower spatial resolution DEM from the same geographical area is introduced. In this way, the sparse representation implements the spatial constraints in the contours and extracts the complementary information from the auxiliary DEM. Furthermore, the proposed method integrates the advantage of the unbiased estimation of kriging. For brevity, the proposed method is called the kriging and sparse spatial regularization (KSSR) method. The performance of the proposed KSSR method is demonstrated by experiments in Shuttle Radar Topography Mission (SRTM) 30 m DEM and Advanced Spaceborne Thermal Emission and Reflection Radiometer (ASTER) 30 m global digital elevation model (GDEM) generation from the corresponding contours and a 90 m DEM. The experiments confirm that the proposed KSSR method outperforms the traditional kriging and SSR methods, and it can be successfully used for DEM generation from contours.



## 1. Introduction

A DIGITAL elevation model (DEM) is an array representation of squared cells (pixels), with an elevation value associated with each pixel (Arun, 2013; Rishikeshan et al., 2014). It represents three-dimensional information of the Earth's surface. Additionally, DEM can also be represented by other forms, such as triangulated irregular network (TIN) and contour maps (Shan and Aparajithan, 2005; Ma, 2005), etc. It is well known that DEMs can help to provide solutions to the theoretical and application-related problems in geosciences. For example, DEMs play an important role in hydrological modeling (Hopkinson et al., 2009; Le Coz et al., 2009; Li et al., 2017), geological studies (Yang et al., 2011; Ricchetti, 2001), disaster analysis (Demirkesen et al., 2007; Tsai et al., 2010), agriculture applications (Tijskens et al., 2003; Bishop and McBratney, 2002), and so on. There are a wide variety of DEM products, and the typical representative examples include the Shuttle Radar Topography Mission (SRTM) digital elevation data and the Advanced Spaceborne Thermal Emission and Reflection Radiometer (ASTER) global digital elevation model (GDEM). SRTM successfully covers over 80% of the Earth's land surface between 60°N and 56°S with data points posted every 1 arc-second (~30 meters) or 3 arc-second (~90 meters). The ASTER GDEM covers more than 99% of land surfaces between 83°N and 83°S and is composed of 22,600 1°-by-1° tiles with a 1 arc-second (30 m) grid of elevation postings. The early DEM generation involved digitizing topographic maps, which has subsequently been accompanied with some other approaches, such as automatic matching of aerial photography, synthetic aperture radar (SAR) interferometry, and laser scanning (Oky et al., 2002; Yue et al., 2015). In other words, the generation of DEMs generally involves data from different sources: contours, photogrammetric data, and field data (Taud et al., 1999). Compared to the other two kinds of data, contours are a cheap data source because, in most countries, they cover the whole area in different scales (Oky et al., 2002).

* Corresponding author at: School of Remote Sensing and Information Engineering, Wuhan University, PR China.
*E-mail addresses:* lixinghua5540@whu.edu.cn (X. Li), shenhf@whu.edu.cn (H. Shen), ruitaofeng@whu.edu.cn (R. Feng), aaronleecool@whu.edu.cn (J. Li), zlp62@whu.edu.cn (L. Zhang).

https://doi.org/10.1016/j.isprsjprs.2017.09.014
0924-2716/

As a result, DEM generation with various data sources has attracted a lot of attention in the research community (Zhou and Zhu, 2013; Shen et al., 2016). According to Taud et al. (1999), the main methods can be classified into two groups: analytic function based methods and direct summation based methods. As far as the analytic function based methods are concerned, the key is to determine the parameters of an assumed parametric surface, and then the height of a given location is evaluated by this function. The representative methods include high-accuracy surface modeling (HASM) Yue et al., 2010 and the parallel projection model (Habib et al., 2004). In contrast, the direct summation based methods do not use a parametric surface, but the estimated elevation is obtained by the known points within the range of influence. This group of methods mainly consists of the various kinds of interpolation methods based on spatial autocorrelation, which means that closer points are more related than farther ones (Tobler's first law of geography). The direct summation based methods include inverse distance weighting (IDW) Lu and Wong, 2008, kriging (Guo et al., 2010), spline interpolation (Soycan and Soycan, 2009), and the radial basis function (RBF) Hofierka et al., 2002. As mentioned above, contours are an inexpensive data source, so generating DEMs from contours is very popular in this field.

In fact, a contour is an isoline which represents a series of points of equal elevation. Since contours have the inherent property of consecutive equivalence and topological property, they can be considered as suitable feature lines to generate DEMs. According to the interpretation of the contours, DEM generation from contours can be classified into two types: point methods and line methods (Oky et al., 2002). The point methods utilize the discrete vertices along the contours to obtain the elevation of unknown grids, which is based on the point characteristics. The two most popular methods are the TIN based method and the minimum curvature method (Oky et al., 2002). In this way, some interpolation methods, such as IDW, kriging, and RBF, can also be used for generating DEMs from contours. In order to calculate the elevation of the grid points, the line methods use all the points along the contours and make use of the line characteristics. For example, flow lines (Maunder, 1999), skeleton lines (Gold, 1999), and intermediate contours (Taud et al., 1999; Takagi and Shibasaki, 1996; Gousie and Franklin, 2003) can all be used to create a DEM. On the one hand, morphological dilation and erosion operations can also be applied in this process (Taud et al., 1999). On the other hand, the correlated information of the contours can also be used for DEM generation. For example, Ardiansyah and Yokoyama (Oky et al., 2002) proposed to interpolate a DEM along the steepest slope perpendicular to a contour. Nowadays, there are a number of tools available for creating DEMs from contours, such as ANUDEM (Hutchinson, 1989), TAPES-G (Gallant and Wilson, 1996), and TOPOG (Vertessy et al., 1994). All these methods can create DEMs from contours, providing results that are generally satisfactory. As we know, contours are generally distributed sparsely. In order to take this trait into consideration, we propose to generate a DEM from contours in the framework of sparse representation.

Sparse representation is a representation that accounts for most or all of the information of a signal by a linear combination of only a small number of elementary signals, called atoms (Li et al., 2015). The redundancy of the signal, which means that the key information in a signal distributes sparsely, lays a solid foundation for the success of sparse representation. Since its appearance in the 1980s, sparse representation can provide a powerful information processing capability, and has been applied in many different fields, e.g., objection recognition (Wright et al., 2009; Agarwal et al., 2004), classification (Zhong et al., 2014; Gui et al., 2014; Iordache et al., 2012; Peng et al., 2015; Zhou et al., 2015), missing information reconstruction (Shen et al., 2014, 2015; Li et al., 2014), denoising (Li et al., 2016; Elad and Aharon, 2006), and information fusion (Li et al., 2013; Calderbank et al., 2011). To the best of our knowledge, there are very few methods that apply sparse representation to generate DEMs. Since sparse representation has an advantage for signal processing with a small amount of information, we attempt here to bring sparse representation into the field of DEM generation.

Iordache et al. (2012) imposed a total variation (TV) regularization constraint on hyperspectral unmixing, and the result was very satisfactory. Inspired by their novel work, we propose the sparse spatial regularization (SSR) method to generate a DEM from contours. In order to obtain a better result, this method needs an auxiliary low spatial resolution (LR) DEM, which becomes the same size as the high spatial resolution (HR) DEM (to be generated) by upsampling. Because of the sparse and parallel distribution of the contours, the spatial constraint may not be enough. On this account, some random unknown elevation points are initially estimated by ordinary kriging. To save time, only a very small number of points from the contours are picked as sample points for kriging. The contours with the interpolated points and the upsampled LR DEM are then permutated using the "image interleaved by line" (IIL) method proposed in our previous work (Li et al., 2016). Finally, the proposed SSR is applied to generate the unknown elevation points. In other words, the calculated elevation points are extracted to form the HR DEM. Generally, a DEM can be represented as a raster-based regular grid or as a vector-based TIN. In this paper, the focus is on raster-format DEM generation.

The rest of this paper is arranged as follows. Section 2 introduces the proposed kriging and sparse spatial regularization (KSSR) method for DEM generation. Section 3 describes the experiments undertaken to assess the effectiveness of DEM generation by the KSSR method. The parameters of KSSR are also analyzed, which is followed by the corresponding conclusions in Section 4.

## 2. Kriging and sparse spatial regularization method

As we all know, contours are a cheap data source for DEM generation, which is where our basic interest lies. In consideration of the sparse distribution of contours and the superiority of sparse representation, we propose to generate a DEM from the contours by the use of the proposed KSSR method. Fig. 1 shows the flow chart of KSSR. The HR contours are partly and randomly interpolated by kriging, and subsequently combined with the resampled LR DEM to form a new DEM. A preliminary result is obtained by nearest neighbor interpolation, which is extracted into patches and reconstructed by SSR. In the following, the three main steps of the proposed KSSR method are introduced. Firstly, the preparatory processing measures are introduced, which contribute to the construction of the model. Secondly, we focus on the SSR DEM generation model. Finally, the solution algorithm is described in detail.

### 2.1. Preparatory processing measures

As shown in Fig. 1, given a raster-format HR contour map $x_1 \in \mathbb{R}^{M_1 \times N_1}$, with $M_1$ representing the column size and $N_1$ representing the row size (the size includes the invalid elevation points), and a raster-format LR DEM $x_2 \in \mathbb{R}^{M_2 \times N_2}$, with $M_2$ and $N_2$ representing the column size and row size, respectively, our target is to obtain an HR DEM $x \in \mathbb{R}^{M_1 \times N_1}$ with the same spatial resolution as $x_1$. The contours are usually distributed in parallel, which limits the ability of sparse representation because the randomness is absent. Therefore, some random unknown elevation points of $x_1$ are estimated by kriging, which is called the "best linear unbiased estimator" (BLUE) Van der Meer, 2012. Kriging has many forms, and ordinary kriging (OK) is taken here as an example. OK amounts

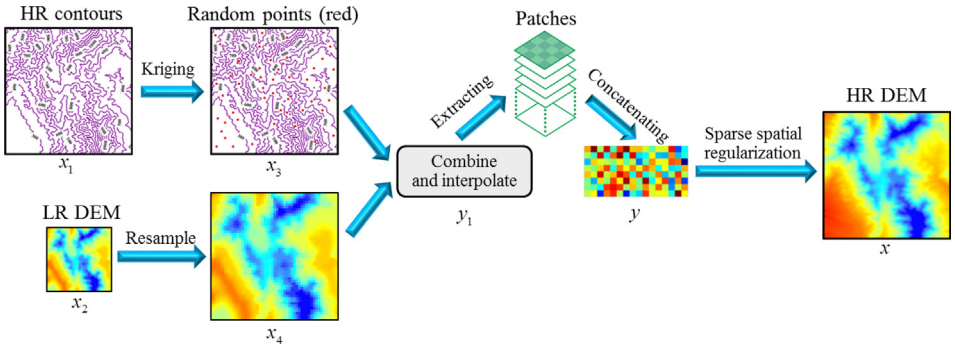


**Fig. 1.** Flow chart of the proposed KSSR method.

to the weighted linear combination of the known samples, whose mathematical expression is:

$$x_1(p_0) = \sum_{i=1}^{K_1} \omega_i x_1(p_i) \tag{1}$$

where $x_1(p_i)$ denotes the elevation value at point $p_i$ of $x_1$ , $p_0$ is the estimated point, $K_1$ is the number of known samples, and $\omega_i$ is the weight satisfying the unbiasedness condition:

$$\sum_{i=1}^{K_1} \omega_i = 1 \tag{2}$$

Additionally, $\omega_i$ also meets the optimality condition, that is, to minimize the variance. By introducing a Lagrange multiplier, this condition can be described as follows:

$$\sum_{i=1}^{n} \omega_i \gamma(p_i - p_j) + \mu = \gamma(p_j - p_0), \quad j = 1, 2, 3, \cdots, n \tag{3}$$

where $\gamma(p_i - p_j)$ represents the value of the semivariance between points $p_i$ and $p_j$ , and $\mu$ is the Lagrange multiplier. The semivariance implies the spatial structure of the variables. When the semivariance is known, the estimated elevation can be obtained using Eqs. (2) and (3). Usually, the semivariance is given by the trend analysis plot of $\gamma(h)$ against the lag interval $h$, and this plot is also called the "experimental semivariogram". The experimental semivariogram can be calculated by the following equation (Bhattacharjee et al., 2014):

$$\gamma(h) = \frac{\sum_{i=1}^{K_2} [x_1(p_i) - x_1(p_i + h)]^2}{2K_2} \tag{4}$$

where $\gamma(h)$ is the semivariance for the lag interval $h$, $p_i$ is the starting point, $p_i + h$ is the end point, and $K_2$ is the number of known samples within the lag interval $h$. If $\gamma(h)$ is only dependent on the length of $h$, but not the direction, it is isotropic. In this study, isotropic kriging is used for simplicity. The experimental semivariogram plot is used for fitting the semivariance model, and can be spherical, exponential, linear, or Gaussian.

In order to save time, only a few points are selected as samples for the kriging interpolation. Via the isotropic kriging interpolation, some random points (usually 20%) are generated. At this time, $x_1$ becomes $x_3$ (see Fig. 1), for which the red points are estimated by kriging. The LR DEM $x_2$ is then upsampled to the same size as $x_1$ by bilinear interpolation. For convenience of description, the upsampled LR DEM is called $x_4 \in \mathbb{R}^{M_1 \times N_1}$ (see Fig. 1). In order to make use of the correlations, $x_3$ and $x_4$ are combined into two-dimensional data as $y_1 \in \mathbb{R}^{2M_1 \times N_1}$. The permutation law of the two pieces of data is the "IIL" method proposed in our previous paper (Li et al., 2016). As with most of the sparse representation methods, the proposed method is also based on patches. The patch extraction operator $R(\cdot)$ extracts a series of patches with the size of $b \times b$, from the upper left to the lower right, with a step size of $l$. At the same time, every patch is converted to a column vector, and all the vectors are concatenated to new two-dimensional data as $y \in \mathbb{R}^{M_3 \times N_3}$ (see Fig. 1), where $M_3 = b^2$ and $N_3 = (2M_1 - b + l) \times (N_1 - b + l)/l^2$ . This extraction process can be mathematically modeled as follows:

$$y = R(y_1) \tag{5}$$

Additionally, the inverse operator of $R(\cdot)$ is defined as:

$$y_1 = R^{-1}(y) \tag{6}$$

where $R^{-1}(\cdot)$ denotes the inverse operator of $R(\cdot)$, which means putting the column-vectorized patches back in their original locations.

### 2.2. The SSR DEM generation model

For brevity, the sparse representation model of DEM generation using the extracted $y$ is first introduced. Let $D \in \mathbb{R}^{b^2 \times m}$ be the dictionary matrix; let $\alpha \in \mathbb{R}^{m \times n}$ be the dictionary coefficients, where $n$ amounts to the number of extracted patches, that is, $n = N_3$; let $\|y\|_F$ be the Frobenius norm of $y$, $\|y\|_F = \sqrt{\text{trace}(yy^T)}$ , trace$(\cdot)$ is the trace norm of the matrix, and $y^T$ is the transpose of $y$ ; and let $\|\alpha\|_{1,1} = \sum_{i=1}^{n} \|\alpha_i\|_1$ , where $\alpha_i$ denotes the $i$th column of $\alpha$ , and $\|\cdot\|_1$ denotes the $\ell_1$ norm of a vector. Assuming that the dictionary $D$ is known, the sparse representation model can be written as follows:

$$\min_{\alpha} \frac{1}{2} \|\Omega D\alpha - y\|_F^2 + \lambda \|\alpha\|_{1,1} \tag{7}$$

where $\Omega$ means the binary label matrix of zeros and ones, with zero representing an unknown elevation point and one representing a known elevation point. $\lambda$ is the regularization parameter. Expression (7) has two terms, in which the first term (data fidelity term) implies the minimum variance, and the second term (regularization term) means the patch sparsity. As we know, $y$ is combined by $x_3$ (HR contours and kriging interpolation result) and $x_4$ (resampled LR DEM), and the dictionary $D$ can be considered as two sub-dictionaries corresponding to $x_3$ and $x_4$. In fact, Expression (7) builds up a connection between the sparse distribution of contours and the sparsity of sparse representation. Based on this kind of priori constraint, we can make a better use of the intrinsic property of the contours. In other words, the generated DEM will be better.

To impose the spatial constraint, TV is introduced, which can promote the piecewise smooth transition of the neighboring elevation points. On the basis of (7), when the TV term is imposed, the expression is transformed into (8):

$$\min_{\alpha} \frac{1}{2} \|\Omega D\alpha - y\|_F^2 + \lambda \|\alpha\|_{1,1} + \lambda_{\text{TV}} \text{TV}(D\alpha) \tag{8}$$

where TV(·) denotes the TV term, and $\lambda_{TV}$ is its regularization parameter. Previous studies have demonstrated that TV-based regularization term can lead to a better restoration than the traditional $\ell_1$ regularization term (Ng et al., 2007), which is our inspiration on the point. Under this circumstance, the generated DEM benefits the sparse constraint and the spatial constraint. As in Iordache et al. (2012), the TV term can be denoted by an operator $H$; hence, (8) has the following form:

$$\min_{\alpha} \frac{1}{2}\|\Omega D\alpha - y\|_F^2 + \lambda\|\alpha\|_{1,1} + \lambda_{TV}\|HD\alpha\|_{1,1} \tag{9}$$

Expression (9) is the proposed SSR model for DEM generation. The solution is described in the next section.

### 2.3. Solution algorithm of the proposed model

We use a method that is similar to the method proposed in Iordache et al. (2012). For the solution of (9), we first translate the objective function into the optimization of the equation constraint in (10):

$$\begin{aligned} \min_{\alpha,V_1,V_2,V_3,V_4} \ & \frac{1}{2}\|V_2 - y\|_F^2 + \lambda\|V_3\|_{1,1} + \lambda_{TV}\|V_4\|_{1,1}, \\ \text{subject to} \ & V_1 = D\alpha \\ & V_2 = \Omega V_1 \\ & V_3 = \alpha \\ & V_4 = HV_1 \end{aligned} \tag{10}$$

Then (10) can be written in the augmented Lagrangian formulation:

$$\begin{aligned} &L(\alpha, V_1, V_2, V_3, V_4, U_1, U_2, U_3, U_4) \\ &= \frac{1}{2}\|V_2 - y\|_F^2 + \lambda\|V_3\|_{1,1} + \lambda_{TV}\|V_4\|_{1,1} \\ &\quad + \frac{\mu}{2}\|D\alpha - V_1 - U_1\|_F^2 + \frac{\mu}{2}\|\Omega V_1 - V_2 - U_2\|_F^2 \\ &\quad + \frac{\mu}{2}\|\alpha - V_3 - U_3\|_F^2 + \frac{\mu}{2}\|HV_1 - V_4 - U_4\|_F^2 \end{aligned} \tag{11}$$

where $U_1$ , $U_2$ , $U_3$ , and $U_4$ are the introduced variables.

The solution of (11) is obtained by decoupling the optimization into three parts: (1) solve variables $\alpha$, $V_1$ , $V_2$ , $V_3$ , and $V_4$ ; (2) update the Lagrange multipliers $U_1$ , $U_2$ , $U_3$ , and $U_4$ ; and (3) update the iteration number. The following describes the details of the solution. Supposing that the variables are all initialized, the variables $\alpha$, $V_1$ , $V_2$ , $V_3$ , and $V_4$ are first solved one after another.

1) Taking the $(k+1)$th iteration, for $\alpha$, the closed-form solution is:

$$\alpha^{(k+1)} = (D^TD + I)^{-1}\left[D^T(V_1^{(k)} + U_1^{(k)}) + V_3^{(k)} + U_3^{(k)}\right] \tag{12}$$

where $I$ is the identity matrix.

2) For $V_1$, the solution is:

$$V_1^{(k+1)} = \left(\Omega^T\Omega + H^TH + I\right)^{-1}\left[\Omega^T\left(V_2^{(k)} + U_2^{(k)}\right) + H^T\left(V_2^{(k)} + U_2^{(k)}\right) + D\alpha^{(k)} - U_1^{(k)}\right] \tag{13}$$

3) The optimization function for $V_2$ is:

$$V_2^{(k+1)} = \frac{1}{1+\mu}\left[y + \mu(\Omega V_1^{(k)} - U_2^{(k)})\right] \tag{14}$$

4) To calculate $V_3$, the problem is the shrinkage operator (Goldstein and Osher, 2009), which is also called soft thresholding:

$$V_3^{(k+1)} = \text{soft}\left(U_3^{(k)} - \alpha^{(k)}, \frac{\lambda}{\mu}\right) \tag{15}$$

where

$$\text{soft}(z,\theta) = \frac{z}{|z|}\max(|z| - \theta, 0) \tag{16}$$

5) For $V_4$, the solution is the soft threshold, as in (15):

$$V_4^{(k+1)} = \text{soft}\left(U_4^{(k)} - HV_1^{(k)}, \frac{\lambda_{TV}}{\mu}\right) \tag{17}$$

6) After the first part is finished, the second part has the following solutions:

$$\begin{aligned} U_1^{(k+1)} &= U_1^{(k)} - D\alpha^{(k+1)} + V_1^{(k+1)} \\ U_2^{(k+1)} &= U_2^{(k)} - \Omega V_1^{(k+1)} + V_2^{(k+1)} \\ U_3^{(k+1)} &= U_3^{(k)} - \alpha^{(k+1)} + V_3^{(k+1)} \\ U_4^{(k+1)} &= U_4^{(k)} - HV_1^{(k+1)} + V_4^{(k+1)} \end{aligned} \tag{18}$$

With Eqs. (12)–(15), (17), and (18), the calculation and update of the variables is completed in the iteration. We repeat this process until it achieves the predetermined iteration number.

## 3. DEM generation experiments and analysis

In order to validate the effectiveness of the proposed KSSR method, a series of simulation experiments was undertaken. In the experiments, two kinds of 30 m DEM (SRTM DEM and ASTER GDEM) were generated from their corresponding contours, with different contour intervals. At the same time, the 90 m DEM products were also used in the generation process. For the purpose of quantitative evaluation, we collected the original 30 m DEMs. In other words, the 30 m DEM products were used for generating the contours and were considered as the evaluation data. The SRTM 30 m and 90 m DEMs were paired as one type of experiment, and the ASTER 30 m and 90 m GDEMs were paired as another type of experiment. The SRTM 90 m products were downloaded from the CGIAR-CSI (Consortium of International Agricultural Research Centers-Consortium for Spatial Information) SRTM 90 m Digital Elevation Database v4.1 (http://www.cgiar-csi.org/data/srtm-90 m-digital-elevation-database-v4-1). The SRTM 30 m products and the ASTER 30 m and 90 m GDEM products were all downloaded from USGS EarthExplorer (http://earthexplorer.usgs.gov/). On the one hand, the effect of the proposed DEM generation method is compared with the results of some other methods. On the other hand, some key factors in the generation result of the proposed KSSR method are analyzed.

The mean absolute error (MAE), root-mean-square error (RMSE), and mean relative error (MRE) are selected as the evaluation indicators. Supposing that $c \in \mathbb{R}^K$ and $d \in \mathbb{R}^K$ are the data to be compared, then the three indicators can be explained with $c$ and $d$. For brevity, we suppose that they are both vectors here. Firstly, the MAE is calculated by the following expression:

$$\text{MAE}(c,d) = \frac{1}{K}\sum_{i=1}^{K}|c_i - d_i| \tag{19}$$

RMSE is defined by:

$$\text{RMSE}(c,d) = \sqrt{\frac{1}{K}\sum_{i=1}^{K}(c_i - d_i)^2} \tag{20}$$

Finally, $d$ is assumed to be the reference data, so the MRE is computed by:

$$\text{MRE}(c,d) = \frac{1}{K}\sum_{i=1}^{K}\frac{|c_i - d_i|}{d_i} \tag{21}$$

### 3.1. Results

The SRTM 30 m DEM was first generated from the 30 m contour map and the corresponding SRTM 90 m DEM. As stated previously, the 30 m contour map was extracted from the original SRTM 30 m DEM. The contour interval was 200 m. Two sub-regions with the size of 12 × 12 km were cropped from the original SRTM 30 m DEM file (s31_w070_1arc_v3), as shown in Figs. 2(a) and 3(a), as were their contours. The latitude and longitude range of Fig. 2(a) is 30.00°∼30.11°S, 69.89°∼70.00°W (located on the border of Argentina and Chile). The latitude and longitude range of Fig. 3 (a) is 30.83°∼30.94°S, 69.56°∼69.67°W (Argentina). The two corresponding SRTM 90 m DEMs were also cropped from the original file "srtm_23_19". To the best of our knowledge, a sparse representation based method for generating DEMs has never previously been reported. Therefore, in consideration of the maturity of the classical kriging interpolation (OK), it was taken as a comparison method. The variogram model was spherical, with a variable range of 50. The HR DEM could be resampled from the LR DEM by bilinear interpolation, which was also taken as a comparison. Additionally, SSR was selected as another kind of contrasting method, in which the random kriging interpolation is removed from KSSR. In other words, the 30 m DEMs were generated from the 30 m contours and 90 m DEM by four methods (kriging, resampling, SRR, and KSSR) in the experiments. Without any special instructions, the parameters of SSR and KSSR were set as follows: $b = 6$ (patch size), $l = 2$ (step size), $m = 256$ (dictionary atom number), $D \in \mathbb{R}^{36\times256}$ (dictionary), $\mu = 0.001$ (introduced regularization parameter in (11)), $\lambda = 0.001$ (sparse regularization parameter), $\lambda_{TV} = 0.005$ (TV regularization parameter), the initial dictionary was obtained by discrete cosine transform (DCT), and the iteration number was 100. In addition, the ratio of the random kriging interpolation was 20% for KSSR. In the following experiments, the influence of different parameters will be evaluated.

The two groups of experiments in which the SRTM 30 m DEMs were generated are shown in Figs. 2 and 3, respectively. As can be seen in the contour maps [Figs. 2(b) and 3(b)], the contours are distributed very sparsely and the elevations vary greatly in the subregions. From the visual effect, all four methods obtain results which are consistent with the original SRTM 30 m DEM [Fig. 2 (a) and 3(a)]. However, after a careful comparison, it can be seen that differences do exist. The kriging obtains a coarse DEM result, with a large number of spatial details missing [see Figs. 2 (c) and 3(c)]. The reason for this is that the sparse contours provide a very weak spatial constraint on the kriging interpolation. Resampling by bilinear interpolation also loses many details, but the degree is not as bad as for kriging [Figs. 2(d) and 3(d)]. Compared to kriging and resampling, SSR obtains many more spatial features, and it benefits from the spatial constraints of the TV regularization and the complementary spatial information from the LR DEM [see Figs. 2(e) and 3(e)]. Although SSR obtains a better result than kriging, missing spatial details still occur. On the other hand, since the contours usually show a regular spatial distribution, this phenomenon has an adverse effect on the reconstruction ability of sparse representation, which is more suitable for a random distribution. As a result, SSR can result in some false outlines along the contours, as can be seen in Fig. 2(e). In order to reduce the influence of the regular distribution, KSSR combines some of the random kriging interpolation on the basis of SSR. As can be seen in Figs. 2(f) and 3(f), KSSR improves the generation result, especially

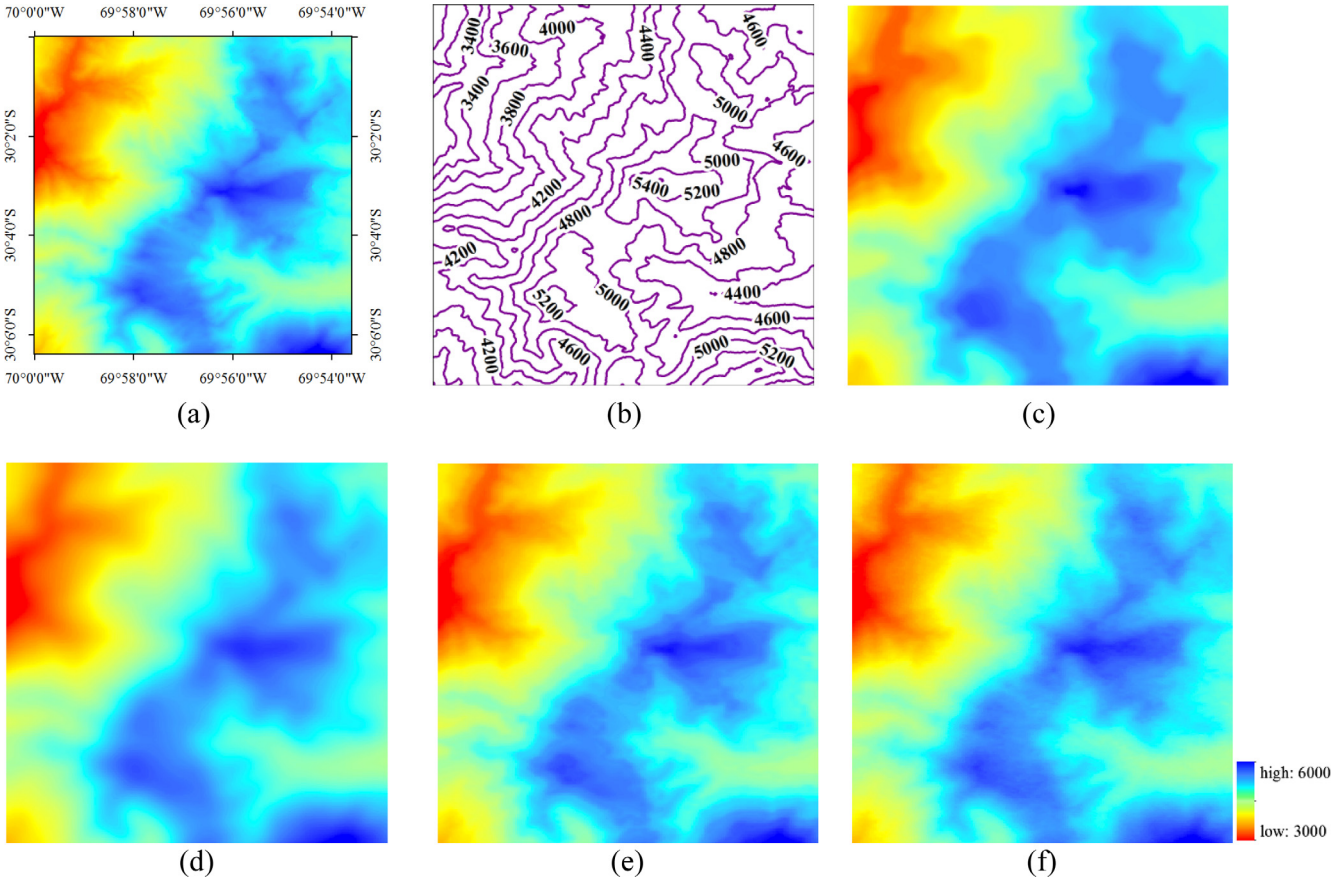


**Fig. 2.** The SRTM 30 m DEM generation results from contours, with a size of 12 × 12 km. (a) The original DEM. (b) The 30 m contour map. (c) Kriging result. (d) Resampling result by LR DEM. (e) SSR result. (f) KSSR result.

in Fig. 2(f). In other words, KSSR produces the best result among the four methods.

The visual effects of the four methods are shown in Figs. 2 and 3. For a deeper understanding, their quantitative assessments from the aspects of MAE, RMSE, and MRE are shown in Table 1. For the three indicators, a lower value means a better accuracy. As we know from Figs. 2 and 3, the elevation of Fig. 2 ranges from about 3000 m to 6000 m, and the elevation of Fig. 3 ranges from about 1500 m to 3500 m. In addition, the contour interval is 200 m. Under the circumstances, the MAEs of the four methods are in the range of a few tens of meters, which implies a satisfactory DEM generation result. For the two groups of experiments, the MAE, RMSE, and MRE decrease according to the order of kriging, resampling/SSR, and KSSR. That is to say, KSSR obtains the best result, which is in accordance with the visual effect. The sparse contours bring an insufficient spatial restriction to the kriging, and it may be that the contour interval is more than the kriging range. Thus, kriging obtains the worst result. Direct DEM generation from another LR DEM by bilinear interpolation also cannot achieve a satisfactory result, because the spatial information is not enough. To this end, SSR imposes a stronger spatial restriction and extracts more useful information from the LR DEM, which is constructive to the result. KSSR makes an improvement on the random distribution of the spatial restriction on the basis of SSR. Therefore, it obtains the best DEM.

After the SRTM 30 m DEM generation experiments, we undertook ASTER 30 m GDEM generation experiments. In these experiments, ASTER 30 m GDEMs were generated from the 30 m contour map and the corresponding ASTER 90 m GDEM. Similarly, the 30 m contour map was extracted from the original ASTER 30 m GDEM. The contour interval was 100 m. Two sub-regions with the size of 12 × 12 km were cropped from the original ASTER 30 m GDEM file (n41_e110_1arc_v3 and n41_e111_1arc_v3), as shown in Figs. 4(a) and 5(a), as were their contours. The latitude and longitude range of Fig. 4(a) is 41.00°∼41.11°N, 110.38°∼110.49°E (China). The latitude and longitude range of Fig. 5(a) is

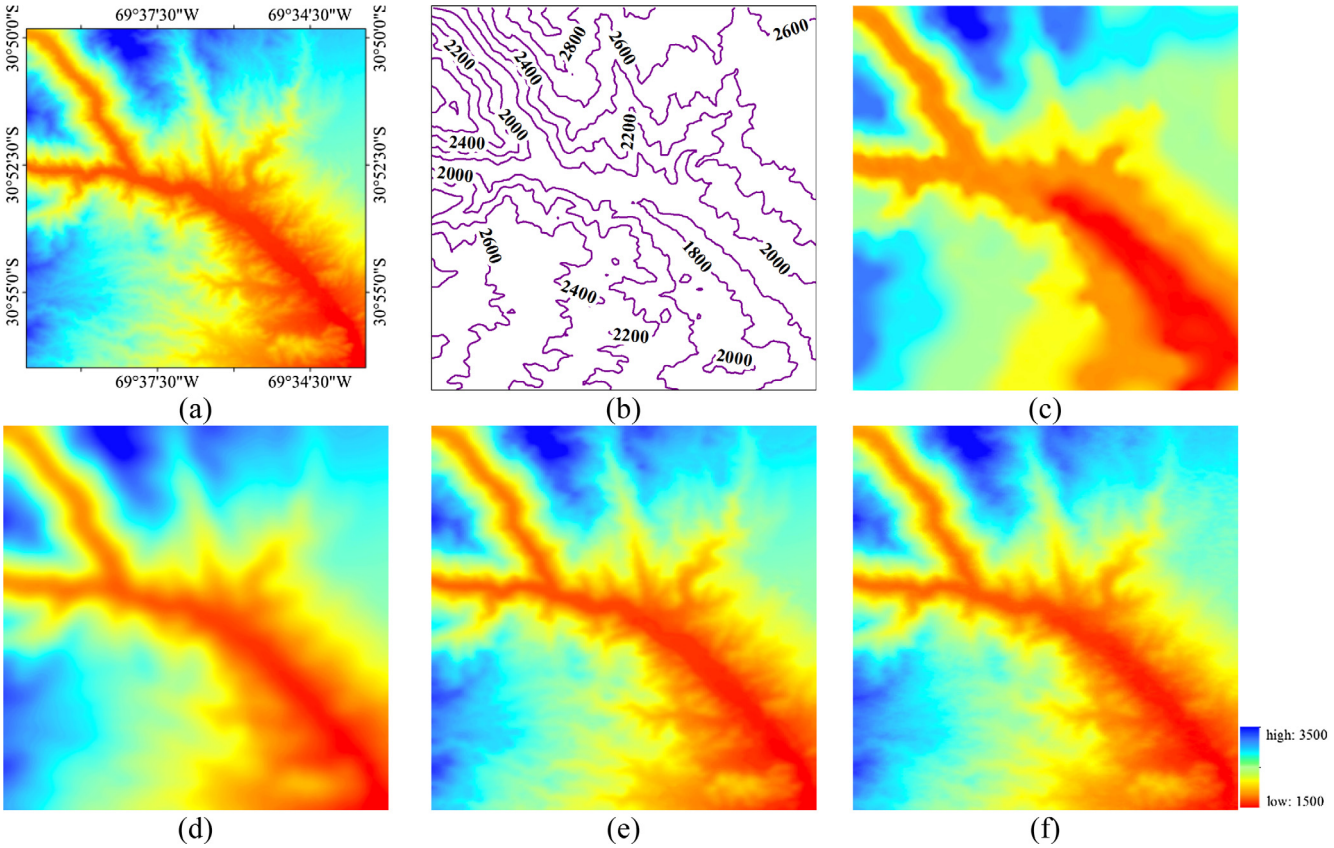


**Fig. 3.** The SRTM 30 m DEM generation results from contours, with a size of 12 × 12 km. (a) The original DEM. (b) The 30 m contour map. (c) Kriging result. (d) Resampling result by LR DEM. (e) SSR result. (f) KSSR result.

**Table 1**
Quantitative evaluation of the DEM generation results from contours (i).

| Images | Methods | MAE | RMSE | MRE/% |
|---|---|---|---|---|
| Fig. 2 | Kriging | 25.9211 | 35.9400 | 0.5816 |
| | Resampling | 21.3019 | 27.4155 | 0.4766 |
| | SSR | 23.8115 | 28.2618 | 0.5214 |
| | KSSR | **12.6037** | **16.1159** | **0.2830** |
| Fig. 3 | Kriging | 36.4478 | 50.5111 | 1.6371 |
| | Resampling | 22.6922 | 29.8660 | 1.0206 |
| | SSR | 13.7390 | 16.6729 | 0.5929 |
| | KSSR | **11.6115** | **14.8839** | **0.5206** |

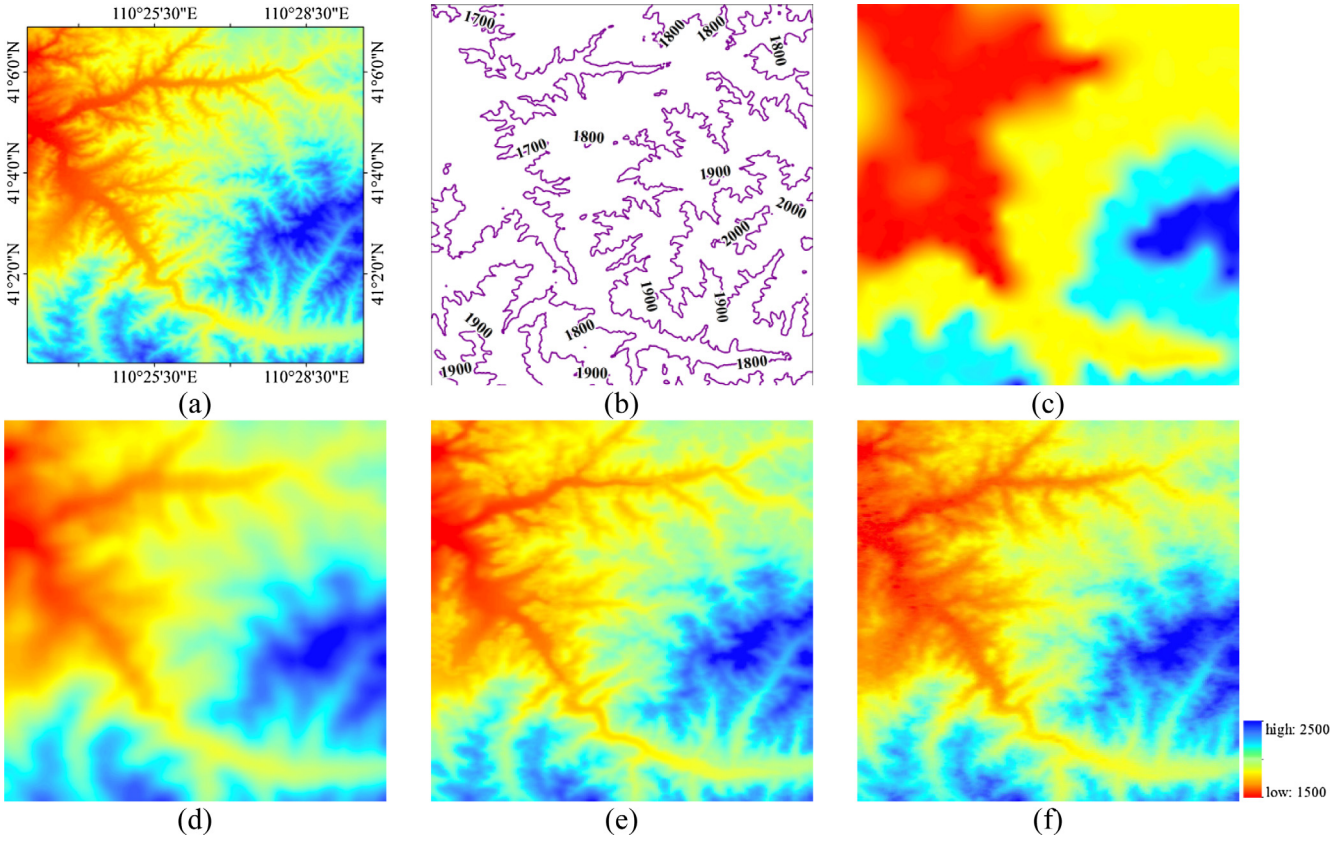


**Fig. 4.** The ASTER 30 m GDEM generation result from contours, with a size of 12 × 12 km. (a) The original DEM. (b) The 30 m contour map. (c) Kriging result. (d) Resampling result by LR DEM. (e) SSR result. (f) KSSR result.

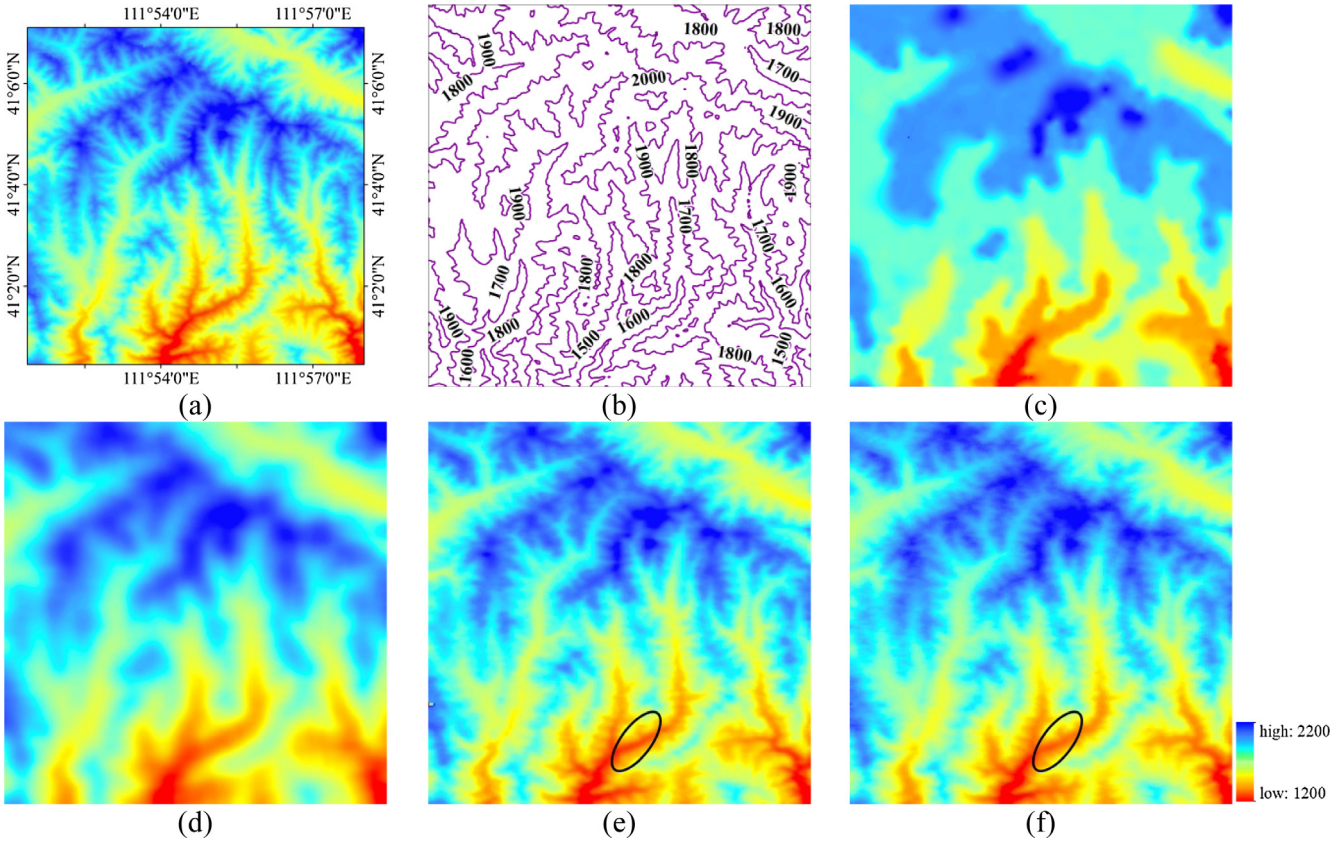


**Fig. 5.** The 30 m GDEM ASTER generation result from contours, with a size of 12 × 12 km. (a) The original DEM. (b) The 30 m contour map. (c) Kriging result. (d) Resampling result by LR DEM. (e) SSR result. (f) KSSR result.

41.01°∼41.12°N, 111.86°∼111.97°E (China).The names of the original two ASTER 90 m GDEM files were "n41_e110_3arc_v3" and "n41_e111_3arc_v3", and the paired sub-regions were cropped from them. Figs. 4 and 5 show the ASTER 30 m GDEM generation results of the two sub-regions by the same four methods. As far as Fig. 4 is concerned, the contours distribute more sparsely than those in Figs. 2 and 3, so kriging obtains an even poorer result, in which almost all the details are missing [Fig. 4(c)]. Resampling from the LR DEM only outperforms kriging by a small degree. This kind of very sparse distribution also results in the effect of SSR being suppressed, and a large amount of noise is introduced [see Fig. 4(e)]. Fortunately, KSSR obtains a satisfactory visual effect [Fig. 4(f)]. As for Fig. 5, the contours are more concentrated, and kriging obtains a better result. KSSR [Fig. 5(f)] again outperforms SSR [Fig. 5(e)], especially in the black ellipse region, where SSR results in obvious errors. The objective evaluation of Figs. 4 and 5 is shown in Table 2, where KSSR again performs better than the other methods. On the whole, these experiments confirm that the proposed KSSR method has an advantage over the traditional methods in terms of DEM generation.

With the help of the previous visual and objective comparisons, the DEM generation effects of the four methods can be established. For a further insight into their generation abilities, we also show the spatial distribution of the generation error. The error is the difference between the original DEM and the generated DEM. In other words, it equates to the generated DEM minus the original DEM. In our opinion, the error contour map reflects the spatial distribution of the error. The error contour maps of Figs. 2–5 are shown in Figs. 6–9, respectively. In these contour maps, the same color was rendering between the neighboring two contour lines. For the same DEM, the same contour line is displayed in the contour map. As can be seen in Figs. 6–9, the numerical error ranges of kriging and resampling are larger than those of SSR and KSSR, indicating that kriging and resampling cause larger DEM errors. In particular, the error contours of SSR and KSSR concentrate around low errors, which represents a better result than kriging and

**Table 2**
Quantitative evaluation of the DEM generation result from contours (ii).

| Images | Methods | MAE | RMSE | MRE/% |
|---|---|---|---|---|
| Fig. 4 | Kriging | 24.8591 | 34.0395 | 1.4091 |
| | Resampling | 11.5703 | 14.1967 | 0.6427 |
| | SSR | 10.1408 | 12.4219 | 0.5677 |
| | KSSR | **7.9971** | **10.2635** | **0.4501** |
| Fig. 5 | Kriging | 21.4199 | 27.8087 | 1.1954 |
| | Resampling | 16.6578 | 20.3480 | 0.9359 |
| | SSR | 11.2295 | 14.0923 | 0.6270 |
| | KSSR | **10.1593** | **12.4640** | **0.5708** |

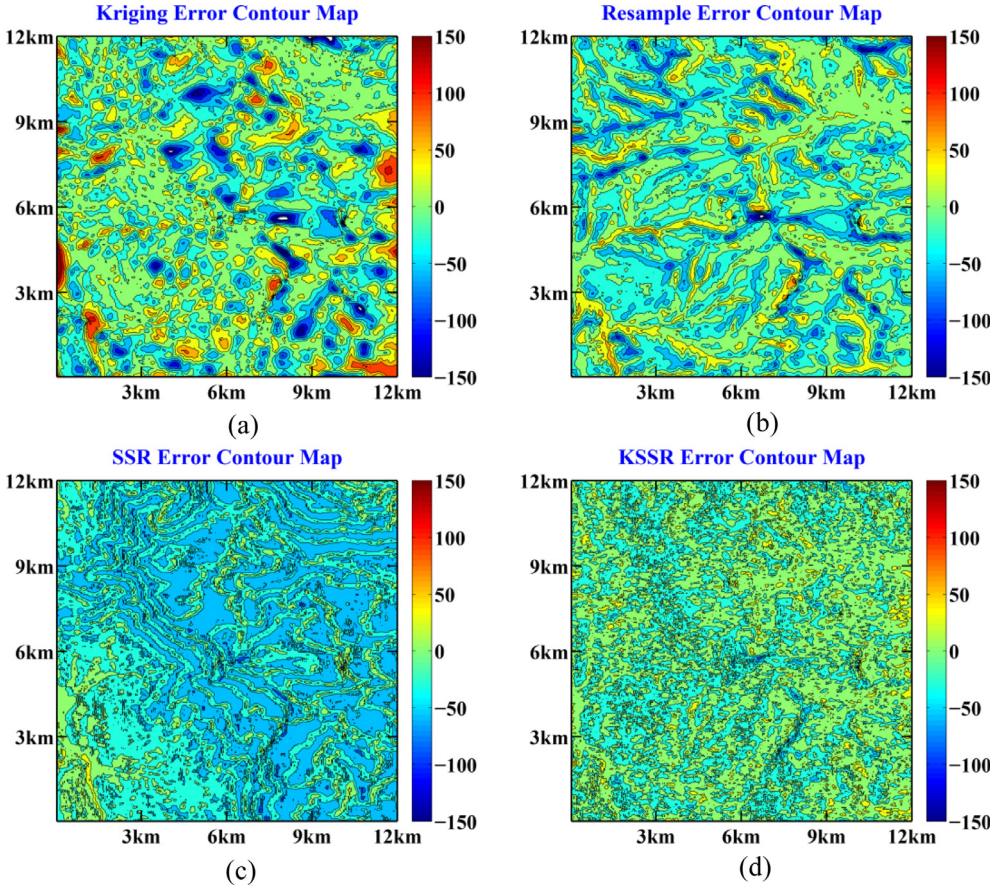


**Fig. 6.** The error contour map of the SRTM DEM generation result obtained by the three methods in Fig. 2. (a) Kriging. (b) Resampling. (c) SSR. (d) KSSR.

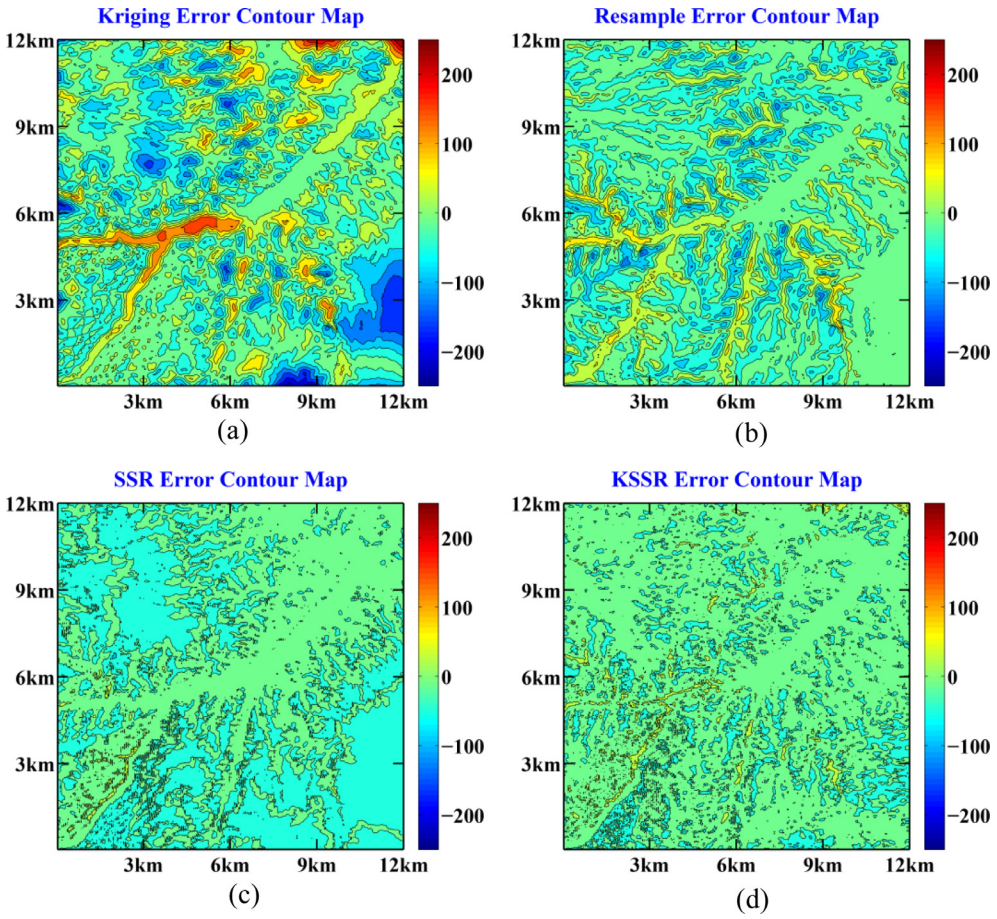


**Fig. 7.** The error contour map of the SRTM DEM generation result obtained by the three methods in Fig. 3. (a) Kriging. (b) Resampling. (c) SSR. (d) KSSR.

resampling. In addition, the error contours of KSSR are more concentrated than those of SSR, indicating that the errors are further refined. In short, the error contour maps also confirm the superiority of the proposed KSSR method.

### 3.2. Parameter analysis

The previous section validated the DEM generation effect of the proposed KSSR method. This section focuses on the parameter analysis of KSSR. The main parameters of KSSR are the size of the extracted patch, the dictionary atom number, the regularization parameters $\lambda$ and $\lambda_{TV}$ , and the iteration number of the solution algorithm. In the following, the parameters are analyzed one after another. It should be explained that the control variate method was adopted in the analysis process. While the current parameter is discussed, the other parameters are kept the same as in Section 3.1.

The first factor to be discussed is the patch size. As with most of the sparse representation based methods, in which the size of the extracted patches has an influence on the result, the patch size of KSSR also affects the DEM generation. In order to reveal the relationship, a series of experiments was conducted with different patch sizes. Without loss of generality, the previous four DEMs in Figs. 2–5 were generated by KSSR, with the patch size varied from $4 \times 4$ to $13 \times 13$. The quantitative evaluation results are shown in Table 3, with the indicators of MAE, RMSE, and MRE. For the four groups of experiments, with the increase in the patch size, the three indicators first decrease, then increase, and finally fluctuate. The relationship is therefore complicated. However, they all share the same phenomenon, in that the optimal DEM generation results are obtained when the patch size is $6 \times 6$. From the four groups of experiments, it is difficult to make the conclusion that a patch size of $6 \times 6$ is the optimal for all DEM generation when KSSR is applied. However, the results do indicate that a patch size of $6 \times 6$ is suitable for 30 m DEM generation from 30 m contours. Large patches may not favor the local correlation of the DEM, and small patches may harm the local unity. The conclusion we can make is that the size should neither be too large nor too small, and a moderate size is the best. In the experiments, the size of $6 \times 6$ obtained the best result when the 30 m DEM was generated from the 30 m contours and the 90 m DEM. As a result, $6 \times 6$ is usually taken as the recommended size for this kind of DEM generation from contours. The performance of our proposed method is fluctuant when the patch size is varying. In fact, the behavior of patch size is related to the contour distribution. With more intensive distribution of contours, the fluctuation will be less obvious. We are also puzzled at present why the performance of patch size varies so greatly. In the future, we will make a deep analysis about it.

In fact, the patch size determines one dimension of the dictionary, and the other dimension of the dictionary is the atom number, which is discussed in the following. In our framework, the atom number should be a square number. To test the effect of the atom number on DEM generation, the KSSR method was applied to generate DEMs with different numbers of atoms. The tested numbers included 10 square numbers, from $10^2$ to $19^2$. The experimental data were the DEMs in Figs. 2–5. Similarly, the DEM generation results with different numbers of atoms are assessed by the indices of MAE, RMSE, and MRE. The quantitative

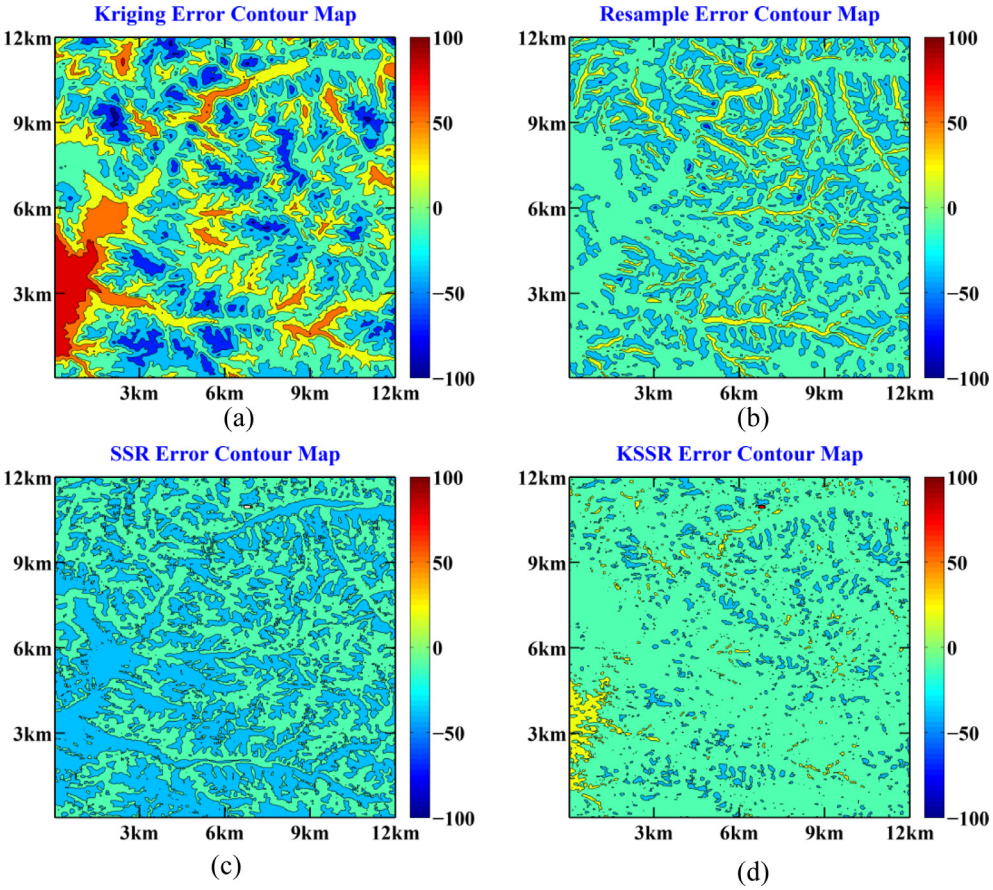


**Fig. 8.** The error contour map of the ASTER GDEM generation result obtained by the three methods in Fig. 4. (a) Kriging. (b) Resampling. (c) SSR. (d) KSSR.

evaluation results are shown in Table 4. As can be seen in Table 4, the indicators change within a certain range when the atom number varies. Figs. 2 and 3 obtain the best result when the atom number is 196, and Figs. 4 and 5 obtain the best result when the atom number is 256. However, when the atom number is 196 or 256, the indicators do not show an obvious difference. Generally, when the atom number is small, the dictionary cannot provide enough signal bases, so that the DEM is generated with large deviations. In contrast, when the atom number is too high, the redundant signal bases may interfere with each other, leading to a decrease in the DEM accuracy. Since the results are more stable between $12^2$ and $16^2$, after the comprehensive consideration, $14^2$ (1 9 6) was more suitable as the dictionary atom number. However, 256 can also obtain a satisfactory result, and it was selected as the dictionary atom number in the experiments (Additionally, 256 is the most used dictionary atom number in the research community of sparse representation).

We now discuss how regularization parameter $\lambda$ influences the result. From Eq. (8), it can be seen that $\lambda$ plays a role in controlling the importance of the sparse coefficients. With the other parameters fixed, KSSR was applied to generate DEMs, with $\lambda$ varying from 0.0001 to 0.01. For brevity, only one representative SRTM DEM and one ASTER GDEM were used in the experiments: Figs. 3 and 5. To visually view the change situation of the DEM generation, the RMSE variation diagram with $\lambda$ is plotted in Fig. 10. As can be seen in Fig. 10, as $\lambda$ varies, for both Figs. 3 and 5, the RMSE first decreases, and then increases. Furthermore, the RMSE achieves the minimum when $\lambda$ equates to 0.001. In other words, with $\lambda$ equal to 0.001, the sparse coefficients obtain an appropriate balance in the SSR model. Therefore, the DEM has the highest generation precision at this time. From Fig. 10, it is clear that $\lambda$ has an important influence on the DEM generation. As a result, it is necessary to choose the optimal $\lambda$ when KSSR is employed. According to our experiments, we recommend setting $\lambda$ as 0.001.

The other regularization parameter, $\lambda_{TV}$ , was analyzed as follows. From Eq. (8), we know that $\lambda_{TV}$ makes a tradeoff between the spatial regularization term and the data fidelity term. In order to reveal the impact of $\lambda_{TV}$ , the RMSE variation diagram with $\lambda_{TV}$ is shown in Fig. 11. The range of $\lambda_{TV}$ is from 0.0001 to 0.01 in Fig. 11. It should be noted that when $\lambda_{TV}$ equates to the first three values (0.0001, 0.0005, and 0.001), KSSR cannot generate a DEM effectively and obtains extremely large RMSE values. For graphical convenience, the RMSE is nominally replaced by 40 and 30, and the red[1] dashed line and blue dashed line are used to represent the extremely large RMSEs of Figs. 3 and 5, respectively. As can be seen in Fig. 11, the RMSE reaches a minimum when $\lambda_{TV}$ has a value of 0.002. As $\lambda_{TV}$ increases, the RMSE stays the same. The experiments demonstrate that $\lambda_{TV}$ is vital to the DEM generation. Compared to $\lambda$, it is easier to determine the optimal $\lambda_{TV}$ . In our experiments, $\lambda_{TV}$ was usually set to 0.005.

The next parameter to be discussed is the iteration number of KSSR. As stated previously, the proposed KSSR method is solved by decoupling the objective function into three parts. The optimized solution is approximated by increasing the iteration number. In the experiments, we recorded the statistics of the RMSE variation for Figs. 3 and 5 when the iteration number was increased from 10 to 140 with an interval of 10. The variation of RMSE is shown in the line chart in Fig. 12. As can be seen in Fig. 12, as the iteration number increases, the RMSE of Figs. 3

[1] For interpretation of color in Figs. 3 and 5, the reader is referred to the web version of this article.

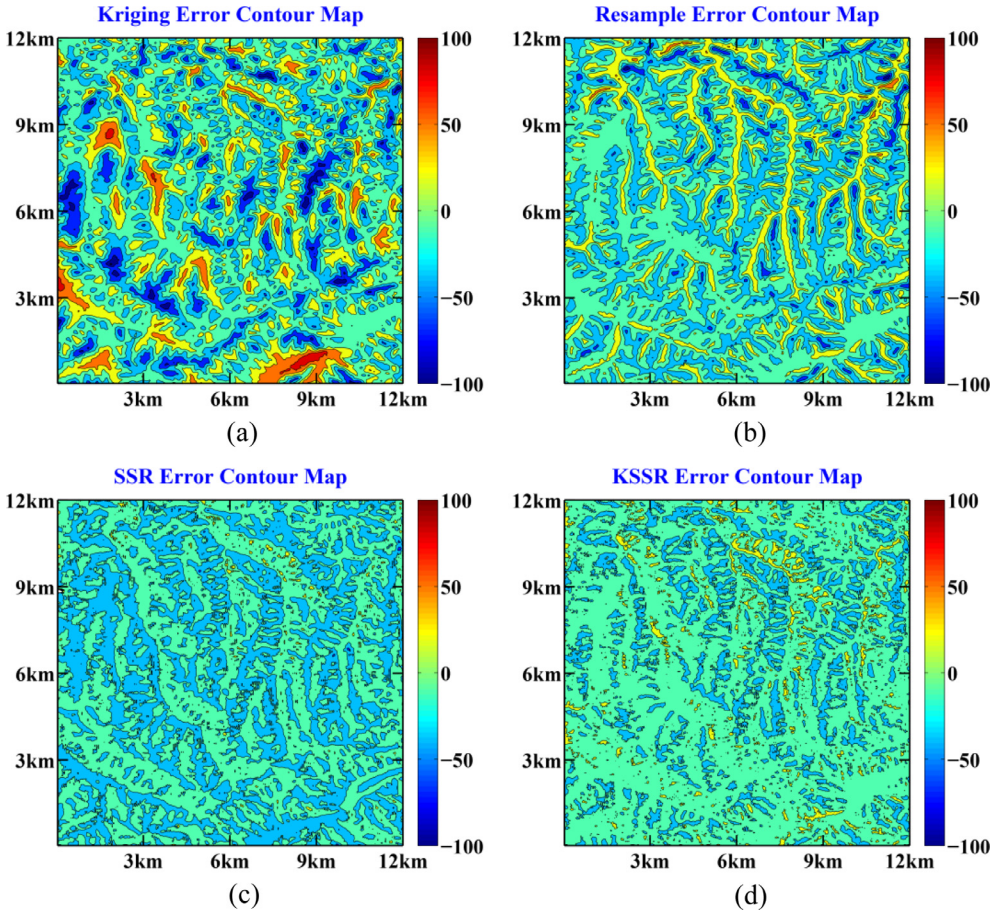


**Fig. 9.** The error contour map of the ASTER GDEM generation result obtained by the three methods in Fig. 5. (a) Kriging. (b) Resampling. (c) SSR. (d) KSSR.

**Table 3**
Quantitative evaluation of different patch sizes.

| Image | Indicator | 4 × 4 | 5 × 5 | 6 × 6 | 7 × 7 | 8 × 8 | 9 × 9 | 10 × 10 | 11 × 11 | 12 × 12 | 13 × 13 |
|---|---|---|---|---|---|---|---|---|---|---|---|
| Fig. 2 | MAE | 66.9561 | 13.7489 | **12.6037** | 52.4202 | 17.0656 | 17.6812 | 18.8946 | 40.8541 | 20.5782 | 22.0432 |
| | RMSE | 81.5401 | 17.7551 | **16.1159** | 66.0834 | 22.0854 | 22.4884 | 24.2252 | 56.8420 | 25.5731 | 28.0427 |
| | MRE/% | 1.4671 | 0.3054 | **0.2830** | 1.1773 | 0.3789 | 0.3950 | 0.4173 | 0.9146 | 0.4566 | 0.4906 |
| Fig. 3 | MAE | 33.9728 | 13.1416 | **11.6115** | 31.3017 | 13.7377 | 14.5630 | 14.5979 | 28.9345 | 15.3515 | 16.8360 |
| | RMSE | 42.4543 | 17.2081 | **14.8839** | 40.8460 | 17.4192 | 18.5479 | 18.5316 | 39.2414 | 19.3602 | 21.1215 |
| | MRE/% | 1.4763 | 0.5821 | **0.5206** | 1.4089 | 0.6107 | 0.6574 | 0.6452 | 1.2773 | 0.6778 | 0.7578 |
| Fig. 4 | MAE | 32.5926 | 8.3750 | **7.9971** | 23.0372 | 10.0289 | 10.6335 | 10.5608 | 18.1951 | 10.5888 | 13.1645 |
| | RMSE | 38.6973 | 11.0266 | **10.2635** | 28.5195 | 12.6697 | 13.6092 | 13.3203 | 24.2201 | 13.3000 | 16.6309 |
| | MRE/% | 1.8060 | 0.4687 | **0.4501** | 1.2752 | 0.5633 | 0.5996 | 0.5895 | 1.0208 | 0.5931 | 0.7430 |
| Fig. 5 | MAE | 29.7238 | 10.3798 | **10.1593** | 23.6878 | 11.6837 | 11.6693 | 12.4298 | 19.9968 | 12.7167 | 13.1175 |
| | RMSE | 35.4031 | 12.9650 | **12.4640** | 29.4184 | 14.3967 | 14.4522 | 15.3683 | 26.4699 | 15.7787 | 16.2612 |
| | MRE/% | 1.6455 | 0.5802 | **0.5708** | 1.3085 | 0.6544 | 0.6562 | 0.6951 | 1.1263 | 0.7091 | 0.7359 |

**Table 4**
Quantitative evaluation of different dictionary atom numbers.

| Image | Indicator | $10^2$ | $11^2$ | $12^2$ | $13^2$ | $14^2$ | $15^2$ | $16^2$ | $17^2$ | $18^2$ | $19^2$ |
|---|---|---|---|---|---|---|---|---|---|---|---|
| Fig. 2 | MAE | 14.9777 | 21.9926 | 12.8725 | 13.5069 | **12.5471** | 13.4964 | 12.6037 | 32.0235 | 22.4435 | 17.6621 |
| | RMSE | 19.4898 | 35.2257 | 16.6756 | 17.4483 | **16.1019** | 17.3413 | 16.1159 | 45.3566 | 30.4903 | 23.1749 |
| | MRE/% | 0.3313 | 0.4818 | 0.2870 | 0.2993 | **0.2786** | 0.2996 | 0.2830 | 0.6806 | 0.4876 | 0.3912 |
| Fig. 3 | MAE | 12.1901 | 16.0416 | 12.0340 | 11.6050 | **11.2359** | 11.6060 | 11.6115 | 18.1459 | 15.3930 | 12.7136 |
| | RMSE | 15.5217 | 22.6636 | 15.3744 | 14.8473 | **14.4524** | 14.8531 | 14.8839 | 24.2756 | 20.6804 | 16.1494 |
| | MRE/% | 0.5393 | 0.7113 | 0.5370 | 0.5142 | **0.4986** | 0.5164 | 0.5206 | 0.7801 | 0.6601 | 0.5631 |
| Fig. 4 | MAE | 9.1913 | 16.9574 | 8.0826 | 8.4167 | 8.0751 | 8.3538 | **7.9971** | 19.4544 | 12.6885 | 9.6340 |
| | RMSE | 11.7119 | 28.6027 | 10.4110 | 10.7068 | 10.3386 | 10.7008 | **10.2635** | 25.1096 | 16.7794 | 12.2845 |
| | MRE/% | 0.5159 | 0.9198 | 0.4516 | 0.4720 | 0.4526 | 0.4683 | **0.4501** | 1.0679 | 0.7056 | 0.5434 |
| Fig. 5 | MAE | 10.9681 | 16.9833 | 10.5049 | 10.5054 | 10.3039 | 10.4320 | **10.1593** | 20.5208 | 14.3606 | 11.2641 |
| | RMSE | 13.4841 | 25.3663 | 12.9858 | 12.9078 | 12.6691 | 12.8269 | **12.4640** | 25.5713 | 18.3663 | 13.8927 |
| | MRE/% | 0.6147 | 0.9270 | 0.5883 | 0.5890 | 0.5774 | 0.5852 | **0.5708** | 1.1279 | 0.8009 | 0.6315 |

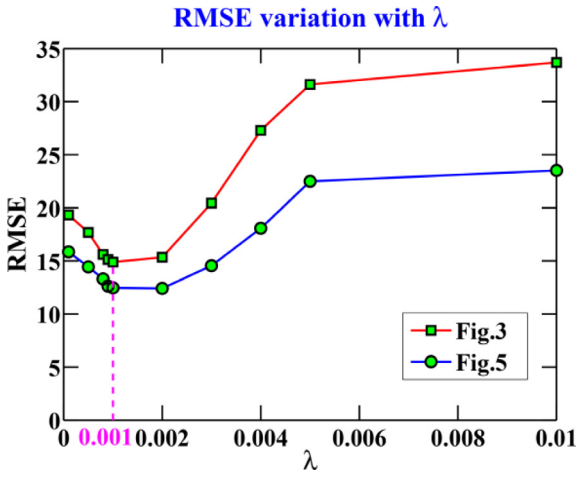


**Fig. 10.** The RMSE variation with $\lambda$ for Figs. 3 and 5.

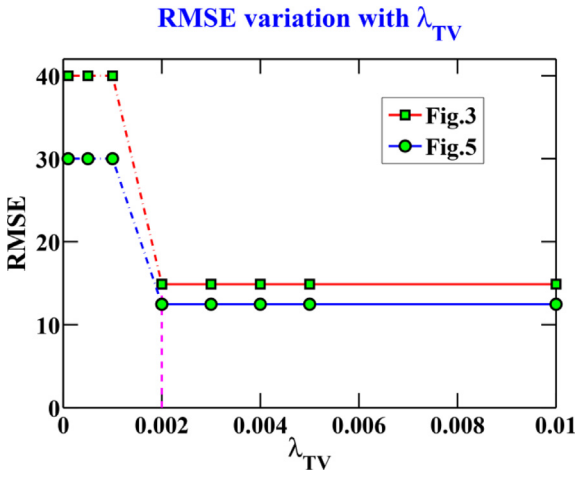


**Fig. 11.** The RMSE variation with $\lambda_{TV}$ for Figs. 3 and 5.

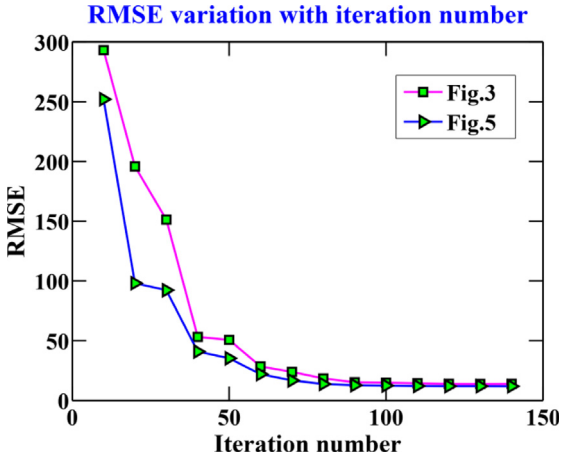


**Fig. 12.** The RMSE variation with iteration number for Figs. 3 and 5.

and 5 clearly decreases. When the iteration number is larger than 100, the decreasing trend is very small and gentle. This phenomenon indicates that the solution is very close to the optimal value. In fact, more iterations means more running time. As a result, to save time, the iteration number was usually set to 100 in the experiments.

## 4. Conclusions

In this paper, we have proposed the KSSR algorithm to generate a DEM from the corresponding contours and another LR DEM. The proposed KSSR makes use of the sparse distribution property of the contours in the framework of sparse representation, with the complementary information extracted from another LR DEM source. Owing to the spatial regularization constraint, the spatial correlation is reinforced. Additionally, some unknown random elevation points are selected and interpolated by kriging, which makes up for the defect of the parallel distribution of the contours. In other words, sparse representation, spatial regularization, and kriging are all utilized in the DEM generation. In the experiments, KSSR was used to generate an SRTM 30 m DEM and an ASTER 30 m GDEM from the 30 m contours. The experimental results confirm that the proposed approach performs well. Compared to SSR and kriging, the proposed KSSR shows obvious advantages, not only qualitatively, but also quantitatively, from the aspects of MAE, RMSE, and MRE. However, KSSR is just an interesting first trial of DEM generation from contours in the framework of sparse representation. The result is preliminary, and there is still much room for improvement. For example, to generate a DEM with the size of 400 $\times$ 400, the time taken is about half an hour, so the time efficiency needs to be improved. Moreover, more kinds of DEM should be tested in experiments. These issues will be addressed in our future work.

## Acknowledgments

This work was supported by the National 863 project of China (2013AA102401), the National Natural Science Foundation of China (NSFC) under Grants Nos. 41701394 and 41422108, the Hubei Natural Science Foundation under Grant No. 2017CFB189, the Open Research Fund of the Key Laboratory of Digital Earth Science, Institute of Remote Sensing and Digital Earth, Chinese Academy of Sciences under Grant No. 2016LDE004, the Open Research Fund of the Key Laboratory of Satellite Mapping Technology and Application, National Administration of Surveying, Mapping and Geoinformation under Grant No. KLSMTA-201703, and China Postdoctoral Science Foundation under Grant No. 2016M602361. The authors would also like to thank the anonymous reviewers.

## References

Agarwal, S., Awan, A., Roth, D., 2004. Learning to detect objects in images via a sparse, part-based representation. IEEE Trans. Pattern Anal. Mach. Intell. 26 (11), 1475–1490.

Arun, P.V., 2013. A comparative analysis of different DEM interpolation methods. Egypt. J. Remote Sens. Space Sci. 16 (2), 133–139.

Bhattacharjee, S., Mitra, P., Ghosh, S.K., 2014. Spatial interpolation to predict missing attributes in GIS using semantic Kriging. IEEE Trans. Geosci. Remote Sens. 52 (8), 4771–4780.

Bishop, T.F.A., McBratney, A.B., 2002. Creating field extent digital elevation models for precision agriculture. Precis. Agric. 3 (1), 37–46.

Calderbank, R., Casazza, P.G., Heinecke, A., Kutyniok, G., Pezeshki, A., 2011. Sparse fusion frames: existence and construction. Adv. Comput. Math. 35 (1), 1–31.

Demirkesen, A.C., Evrendilek, F., Berberoglu, S., Kilic, S., 2007. Coastal flood risk analysis using Landsat-7 ETM+ Imagery and SRTM DEM: A Case Study of Izmir, Turkey. Environ. Monitor. Assess. 131 (1), 293–300.

Elad, M., Aharon, M., 2006. Image denoising Via sparse and redundant representations over learned dictionaries. IEEE Trans. Image Process. 15 (12), 3736–3745.

Gallant, J.C., Wilson, J.P., 1996. TAPES-G: a grid-based terrain analysis program for the environmental sciences. Comput. Geosci. 22 (7), 713–722.

Gold, C., 1999. Crust and anti-crust: a one-step boundary and skeleton extraction algorithm". In: The 15th Annual Symposium on Computational Geometry. Miami Beach, USA, pp. 189–196.

Goldstein, T., Osher, S., 2009. The split Bregman method for L1-regularized problems. SIAM J. Imaging Sci. 2 (2), 323–343.

Gousie, M.B., Franklin, W.R. 2003. Constructing a DEM from Grid-based data by computing intermediate contours. In: The 11th ACM International Symposium on Advances in Geographic Information Systems, New Orleans, Louisiana, USA, pp. 71–77.

Gui, J., Tao, D., Sun, Z., Luo, Y., You, X., Tang, Y.Y., 2014. Group sparse multiview patch alignment framework with view consistency for image classification. IEEE Trans. Image Process. 23 (7), 3126–3137.
Guo, Q., Li, W., Yu, H., Alvarez, O., 2010. Effects of topographic variability and lidar sampling density on several DEM interpolation methods. Photogram. Eng. Remote Sens. 76 (6), 701–712.
Habib, A., Kim, E.M., Morgan, M., and Couloigner, I. 2004. DEM generation from high resolution satellite imagery using parallel projection model. In: the XXth ISPRS Congress, Istanbul, Turkey, pp. 393–398.
Hofierka, J., Parajka, J., Mitasova, H., Mitas, L., 2002. Multivariate interpolation of precipitation using regularized spline with tension. Trans. GIS 6 (2), 135–150.
Hopkinson, C., Hayashi, M., Peddle, D., 2009. Comparing alpine watershed attributes from LiDAR, photogrammetric, and contour-based digital elevation models. Hydrol. Processes 23 (3), 451–463.
Hutchinson, M.F., 1989. A new procedure for gridding elevation and stream line data with automatic removal of spurious pits. J. Hydrol. 106 (3), 211–232.
Iordache, M.D., Bioucas-Dias, J.M., Plaza, A., 2012. Total variation spatial regularization for sparse hyperspectral unmixing. IEEE Trans. Geosci. Remote Sens. 50 (11), 4484–4502.
Le Coz, M., Delclaux, F., Genthon, P., Favreau, G., 2009. Assessment of Digital Elevation Model (DEM) aggregation methods for hydrological modeling: Lake Chad basin, Africa. Comput. Geosci. 35 (8), 1661–1670.
Li, S., Yin, H., Fang, L., 2013. Remote sensing image fusion via sparse representations over learned dictionaries. IEEE Trans. Geosci. Remote Sens. 51 (9), 4779–4789.
Li, X., Shen, H., Zhang, L., Zhang, H., Yuan, Q., Yang, G., 2014. Recovering quantitative remote sensing products contaminated by thick clouds and shadows using multitemporal dictionary learning. IEEE Trans. Geosci. Remote Sens. 52 (11), 7086–7098.
Li, X., Shen, H., Zhang, L., Li, H., 2015. Sparse-based reconstruction of missing information in remote sensing images from spectral/temporal complementary information. ISPRS J. Photogram. Remote Sens. 106, 1–15.
Li, J., Yuan, Q., Shen, H., Zhang, L., 2016. Noise removal from hyperspectral image with joint spectral-spatial distributed sparse representation. IEEE Trans. Geosci. Remote Sens. 54 (9), 5425–5439.
Li, X., Shen, H., Li, H., Zhang, L., 2016. Patch matching-based multitemporal group sparse representation for the missing information reconstruction of remote-sensing images. IEEE J. Select. Topics Appl. Earth Observ. Remote Sens. 9 (8), 3629–3641.
Li, X., Fu, W., Shen, H., Huang, C., Zhang, L., 2017. Monitoring snow cover variability (2000–2014) in the Hengduan Mountains based on cloud-removed MODIS products with an adaptive spatio-temporal weighted method. J. Hydrol. 551, 314–327.
Lu, G.Y., Wong, D.W., 2008. An adaptive inverse-distance weighting spatial interpolation technique. Comput. Geosci. 34 (9), 1044–1055.
Ma, R., 2005. DEM generation and building detection from Lidar data. Photogram. Eng. Remote Sens. 71 (7), 847–854.
Maunder, C.J., 1999. An automated method for constructing contour-based digital elevation models. Water Resour. Res. 35 (12), 3931–3940.
Ng, M.K., Shen, H., Zhang, L., Lam, E., 2007. A total variation based super-resolution reconstruction algorithm for digital video. EURASIP J. Adv. Signal Process. 2007, 1–16. no. Article ID 74585.
Oky, P., Ardiansyah, Dicky, Yokoyama, R., 2002. DEM generation method from contour lines based on the steepest slope segment chain and a monotone interpolation function. ISPRS J. Photogram. Remote Sens. 57 (1–2), 86–101.
Peng, J., Zhou, Y., Chen, C.L.P., 2015. Region-Kernel-based support vector machines for hyperspectral image classification. IEEE Trans. Geosci. Remote Sens. 53 (9), 4810–4824.
Ricchetti, E., 2001. Visible-infrared and radar imagery fusion for geological application: a new approach using DEM and sun-illumination model. Int. J. Remote Sens. 22 (11), 2219–2230.
Rishikeshan, C.A., Katiyar, S.K., Mahesh, V.N.V. 2014. Detailed evaluation of DEM interpolation methods in GIS using DGPS data, In: the 6th International Conference on Computational Intelligence and Communication Networks (CICN), Bhopal, India, pp. 666–671.
Shan, J., Aparajithan, S., 2005. Urban DEM generation from Raw Lidar data. Photogram. Eng. Remote Sens. 71 (2), 217–226.
Shen, H., Li, X., Zhang, L., Tao, D., Zeng, C., 2014. Compressed sensing-based inpainting of aqua moderate resolution imaging spectroradiometer band 6 using adaptive spectrum-weighted sparse bayesian dictionary learning. IEEE Trans. Geosci. Remote Sens. 52 (2), 894–906.
Shen, H., Li, X., Cheng, Q., Zeng, C., Yang, G., Li, H., Zhang, L., 2015. Missing information reconstruction of remote sensing data: a technical review. IEEE Geosci. Remote Sens. Magazine 3 (3), 61–85.
Shen, H., Meng, X., Zhang, L., 2016. An integrated framework for the spatio-temporal-spectral fusion of remote sensing images. IEEE Trans. Geosci. Remote Sens. 54 (12), 7135–7148.
Soycan, A., Soycan, M., 2009. Digital elevation model production from scanned topographic contour maps via thin plate spline interpolation. Arab. J. Sci. Eng. 34 (1), 121–134.
Takagi, M., Shibasaki, R., 1996. An interpolation method for continental DEM generation using small scale contour maps. Int. Archives Photogram. Remote Sens. 31, 847–852.
Taud, H., Parrot, J.-F., Alvarez, R., 1999. DEM generation by contour line dilation. Comput. Geosci. 25 (7), 775–783.
Tijskens, E., Ramon, H., Baerdemaeker, J.D., 2003. Discrete element modelling for process simulation in agriculture. J. Sound Vib. 266 (3), 493–514.
Tsai, F., Hwang, J.-H., Chen, L.-C., Lin, T.-H., 2010. Post-disaster assessment of landslides in southern Taiwan after 2009 Typhoon Morakot using remote sensing and spatial analysis. Natural Hazards Earth Syst. Sci. 10 (10), 2179–2190.
Van der Meer, F., 2012. Remote-sensing image analysis and geostatistics. Int. J. Remote Sens. 33 (18), 5644–5676.
Vertessy, R., O'Loughlin, E., Beverly, C., Butt, A. 1994. Australian experiences with the CSIRO Topog model in land and water resources management. In: UNESCO International Symposium on Water Resources Planning in a Changing World, Karlsruhe, Germany, pp. 135–144.
Wright, J., Yang, A.Y., Ganesh, A., Sastry, S.S., Ma, Y., 2009. Robust face recognition via sparse representation. IEEE Trans. Pattern Anal. Mach. Intell. 31 (2), 210–227.
Yang, L., Meng, X., Zhang, X., 2011. SRTM DEM and its application advances. Int. J. Remote Sens. 32 (14), 3875–3896.
Yue, T.-X., Song, D.-J., Du, Z.-P., Wang, W., 2010. High-accuracy surface modelling and its application to DEM generation. Int. J. Remote Sens. 31 (8), 2205–2226.
Yue, L., Shen, H., Yuan, Q., Zhang, L., 2015. Fusion of multi-scale DEMs using a regularized super-resolution method. Int. J. Geograph. Inform. Sci. 29 (12), 2095–2120.
Zhong, Y., Feng, R., Zhang, L., 2014. Non-local sparse unmixing for hyperspectral remote sensing imagery. IEEE J. Select. Topics Appl. Earth Observ. Remote Sens. 7 (6), 1889–1909.
Zhou, Q., Zhu, A.X., 2013. The recent advancement in digital terrain analysis and modeling. Int. J. Geograph. Inform. Sci. 27 (7), 1269–1271.
Zhou, Y., Peng, J., Chen, C.L.P., 2015. Dimension reduction using spatial and spectral regularized local discriminant embedding for hyperspectral image classification. IEEE Trans. Geosci. Remote Sens. 53 (2), 1082–1095.